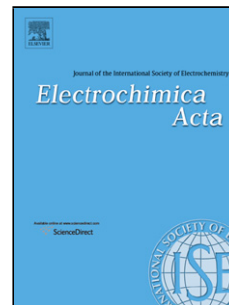


## Accepted Manuscript

Title: Hierarchical mesoporous  $\gamma$ -Fe<sub>2</sub>O<sub>3</sub>/carbon nanocomposites derived from metal organic frameworks as a cathode electrocatalyst for rechargeable Li-O<sub>2</sub> batteries

Author: Wei Chen Zhian Zhang Weizhai Bao Yanqing Lai Jie Li Yongqing Gan Jianjun Wang



PII: S0013-4686(14)00870-6  
DOI: <http://dx.doi.org/doi:10.1016/j.electacta.2014.04.110>  
Reference: EA 22616

To appear in: *Electrochimica Acta*

Received date: 2-1-2014  
Revised date: 25-3-2014  
Accepted date: 20-4-2014

Please cite this article as: W. Chen, Z. Zhang, Y. Lai, J. Li, Y. Gan, J. Wang, Hierarchical mesoporous  $\gamma$ -Fe<sub>2</sub>O<sub>3</sub>/carbon nanocomposites derived from metal organic frameworks as a cathode electrocatalyst for rechargeable Li-O<sub>2</sub> batteries, *Electrochimica Acta* (2014), <http://dx.doi.org/10.1016/j.electacta.2014.04.110>

This is a PDF file of an unedited manuscript that has been accepted for publication. As a service to our customers we are providing this early version of the manuscript. The manuscript will undergo copyediting, typesetting, and review of the resulting proof before it is published in its final form. Please note that during the production process errors may be discovered which could affect the content, and all legal disclaimers that apply to the journal pertain.

# Hierarchical mesoporous $\gamma$ -Fe<sub>2</sub>O<sub>3</sub>/carbon nanocomposites derived from metal organic frameworks as a cathode electrocatalyst for rechargeable Li-O<sub>2</sub> batteries

Wei Chen, Zhian Zhang\*, Weizhai Bao, Yanqing Lai\*, Jie Li, Yongqing Gan, Jianjun Wang

*School of Metallurgy and Environment, Central South University, Changsha Hunan 410083, China*

## Abstract

Hierarchical mesoporous  $\gamma$ -Fe<sub>2</sub>O<sub>3</sub>/carbon nanocomposites were prepared from metal organic frameworks (MOFs) MIL-100(Fe). The  $\gamma$ -Fe<sub>2</sub>O<sub>3</sub>/carbon nanocomposites and its precursor MIL-100(Fe) was characterized by X-ray diffraction (XRD), X-ray photoelectron spectroscopy (XPS), Raman spectra (Raman), field emission scanning electron microscopy (SEM), transmission electron microscopy (TEM), thermogravimetry analysis (TGA) and N<sub>2</sub> adsorption/desorption measurements. It is found that the as-prepared materials possess a hierarchical mesoporous nanostructure between the carbon and  $\gamma$ -Fe<sub>2</sub>O<sub>3</sub> nanoparticles. When applied as cathode catalysts in rechargeable Li-O<sub>2</sub> batteries, it is demonstrated from the galvanostatic discharge-charge process and cyclic voltammetry (CV) that the electrode with  $\gamma$ -Fe<sub>2</sub>O<sub>3</sub>/carbon nanocomposites exhibits a lower charge and discharge over-potential, higher discharge capacity and better cycling stability than the pure Super P electrode, indicating its potential as a promising catalyst for Li-O<sub>2</sub> batteries. The electrode with  $\gamma$ -Fe<sub>2</sub>O<sub>3</sub>/carbon nanocomposites shows a discharge capacity up to ~5970 mAh g<sup>-1</sup><sub>carbon+catalyst</sub> at 0.1 mA cm<sup>-2</sup> and a high C-rate performance, and exhibits a very stable discharge voltage plateau of 2.7 V and a charge voltage plateau of ~3.75V. With the addition of  $\gamma$ -Fe<sub>2</sub>O<sub>3</sub>/carbon nanocomposites, the Li-O<sub>2</sub> batteries can obtain good cycle performance over 30

---

\* Corresponding author: Tel: +86 731 88830649; Fax: +86 731 88830649.

E-mail address: [zza75@163.com](mailto:zza75@163.com) (Z. Zhang); [laiyanqingcsu@163.com](mailto:laiyanqingcsu@163.com) (Y. Lai).

cycles as confining the discharge/charge capacities to  $600 \text{ mA h g}^{-1}_{\text{carbon+catalyst}}$ .

**Keywords:** MOFs; Li-O<sub>2</sub> batteries; electrocatalyst;  $\gamma$ -Fe<sub>2</sub>O<sub>3</sub>/carbon

## 1. Introduction

Rechargeable non-aqueous lithium-O<sub>2</sub> batteries have received more and more academic and technological attention due to their extremely high theoretical specific energy of  $11,140 \text{ Wh kg}^{-1}$  excluding oxygen and  $3458 \text{ Wh kg}^{-1}$  including oxygen, which is 5-10 times higher than that of conventional lithium-ion batteries [1-3]. However, there are still a lot of challenges that must be addressed before the practical application of the Li-O<sub>2</sub> batteries. One of the critical challenges is the slow kinetic of the oxygen reaction resulting in large over-potentials, especially in the oxygen evolution reaction (OER) direction [4]. The possible solution on reducing the over-voltage is adding a catalyst for the oxygen reduction reaction (ORR) and OER [5, 6]. Several types of catalysts, including noble metals [7, 8], metal complexes [9], transitional metal oxides [10-12] and nanocomposites [13, 14] have been demonstrated as efficient catalysts for the electrochemical reactions in the Li-O<sub>2</sub> batteries. Although the high intrinsic catalytic activity of a catalyst is a critical factor to facilitate the performance of Li-O<sub>2</sub> batteries, the morphology also has a great influence on its performance. Bulk catalyst usually exhibits limited catalytic activity probably because of their large particle size and low specific surface area. As well-known, highly efficient catalyst needs high surface areas and more active sites, that can be provided by porous nanostructures [15-17]. Oh et al. obtained a metallic mesoporous pyrochlore that showed a great electro-catalytically active as a catalyst for lithium-O<sub>2</sub> batteries [15]. Zhao et al. synthesized hierarchical mesoporous perovskite  $\text{La}_{0.5}\text{Sr}_{0.5}\text{CoO}_{2.91}$  (LSCO) nanowires and found that they exhibited a higher electrocatalytic active than LSCO nanoparticles [16]. Apart from this, the high

electronic conductivity is also important for the catalyst to possess higher electrocatalytic active [15, 17-19]. Therefore, carbon-supported catalyst nanoparticles have been developed to enhance the electrocatalytic activity [17]. However, there has been limited success in finding relatively simple ways to produce porous transition metal oxides/carbon nanocomposites catalyst, which have both porous structures to obtain more active sites and a certain amount of carbon to increase electronic conductivity.

Metal organic frameworks (MOFs), built from metal ions and organic ligands, have emerged as a promising class of porous crystalline materials not only because of the very large specific surface area and ultrahigh porosity, but also due to their potential applications in gas storage and separation, semiconductor material, catalysis, etc [20-22]. Recently, Because of the presence of organic ligands and the evenly distribution of metal ions in the robust MOF structures, their high specific surface area and porosity, MOFs have been recognized as very promising precursors for the synthesis of carbon based porous nanocomposites materials, such as porous carbon materials [23] and porous metal oxide nanomaterials [24]. For instance, Yang et al. used MOF-5 to prepare porous carbon through carbonization [23]. Xu et al. reported a synthesis of a spindle-like mesoporous  $\alpha$ -Fe<sub>2</sub>O<sub>3</sub> by thermal treatment of MOFs [24]. To the best of our knowledge, as of yet there has been very limited reports on using MOFs as the template to prepare porous nanocomposites materials as the catalyst for Li-O<sub>2</sub> batteries.

As an attractive alternative to precious metal catalyst, iron oxide have been considered as one of the most promising catalysts due to their very high abundance, low cost, environmental friendliness and excellent catalytic performance for both ORR and OER. It has attracted extensive attention for potential applications in fuel cell and Li-O<sub>2</sub> battery [18, 25]. Zhang et al. [18]

synthesized  $\text{Fe}_2\text{O}_3/\text{graphene}$  via an electrochemical process as cathode in  $\text{Li-O}_2$  batteries, which presented excellent electrochemical properties. Lu et al. uniformly dispersed  $\text{Fe}_3\text{O}_4/\text{Fe}$  nanocomposites on porous carbon and took the materials as cathode in  $\text{Li-O}_2$  batteries that exhibited good electrochemical behavior in cell tests [25]. As one of the iron oxides family,  $\gamma\text{-Fe}_2\text{O}_3$  is widely applied as catalyst in many fields, which indicates the good intrinsic catalytic activity of  $\gamma\text{-Fe}_2\text{O}_3$  [26-27]. However, there are no reports about using  $\gamma\text{-Fe}_2\text{O}_3$  as a catalyst for  $\text{Li-O}_2$  batteries.

Here, in this work, we report a rational design and synthesis of a hierarchical mesoporous  $\gamma\text{-Fe}_2\text{O}_3/\text{carbon}$  nanocomposites catalyst using unique metal organic frameworks ( $\text{MIL-100(Fe)}$ ) as precursor. The  $\gamma\text{-Fe}_2\text{O}_3/\text{carbon}$  nanocomposites catalyst prepared via pyrolysis of  $\text{MIL-100(Fe)}$  was loaded onto Super P to fabricate the cathode for promoting the ORR and OER in non-aqueous lithium- $\text{O}_2$  batteries. Carbonizing  $\text{MIL-100(Fe)}$  proposes a new simple method for preparing catalyst in lithium- $\text{O}_2$  batteries, which will lead to the development of an effective and low cost fabricating strategy that has high potential for scaling up. Because of the unique structure and composition of the porous  $\gamma\text{-Fe}_2\text{O}_3/\text{carbon}$  nanocomposites catalyst, the  $\text{O}_2$  electrode with the as-prepared catalyst shows an obviously improved electrochemical performance, including lower over-potential, higher capacity, and better cycle performance. These results show that  $\gamma\text{-Fe}_2\text{O}_3/\text{carbon}$  nanocomposites catalyst prepared by the pyrolysis of  $\text{MIL-100(Fe)}$  is a promising catalyst material for ORR and OER in the lithium- $\text{O}_2$  batteries.

## 2. Experimental

### 2.1. Materials

1,3,5-Benzenetricarboxylic acid ( $\text{H}_3\text{BTC}$ ) was purchased from Adamas-beta, and ferric

chloride hexahydrate ( $\text{FeCl}_3 \cdot 6\text{H}_2\text{O}$ ), HF and  $\text{HNO}_3$  were purchased from Sinopharm (Shanghai) Chemical Reagent Co., Ltd., China. Other chemical reagents were analytical grade, obtained from commercial suppliers, and used without any further purification.

## 2.2. Synthesis of MIL-100(Fe)

MIL-100(Fe) was prepared by following the synthetic hydrothermal procedure described in the previously literature [28]. 2.457 g of  $\text{FeCl}_3 \cdot 6\text{H}_2\text{O}$  (9 mmol) and 1.275 g of  $\text{H}_3\text{BTC}$  (6 mmol) were mixed in 40 mL deionized water, then HF (18 mmol) and  $\text{HNO}_3$  (5.42 mmol) were carefully added to the solution. After vigorously stirring for an hour, the solution was transferred into a Teflon autoclave. The autoclave was placed in an oven at  $170^\circ\text{C}$  for 18 h. After cooling down to room temperature, the product was collected by centrifugation, and further purified by using hot water and ethanol for three times, respectively. The orange solid of MIL-100(Fe) was finally obtained after drying in a vacuum oven at  $70^\circ\text{C}$  for 24 h.

## 2.3. Synthesis of $\gamma\text{-Fe}_2\text{O}_3$ /carbon nanocomposites

The porous  $\gamma\text{-Fe}_2\text{O}_3$ /carbon nanocomposites materials were synthesized using MIL-100(Fe) as a Fe/C precursor and a template. The dried MIL-100(Fe) was put into a tube furnace in a ceramic boat and heated to  $600^\circ\text{C}$  under argon atmosphere at a heating rate of  $5^\circ\text{C}/\text{min}$  and held at this temperature for 5 h. After cooling to room temperature, the generated  $\gamma\text{-Fe}_2\text{O}_3$ /carbon nanocomposites were harvested.

## 2.4. Materials characterizations

Powder X-ray diffraction (XRD) patterns were obtained by using a Rigaku D/Max 2500 equipped with a graphite-monochromated Cu  $K\alpha$  radiation source. Field emission scanning electron microscopy (SEM) images were obtained by using Nova NanoSEM 230. Transmission

electron microscopy (TEM) images were taken on Tecnai G2 20ST. Thermogravimetric analysis (TGA) was performed on SDTQ600. Raman spectra (Raman) was measured on a Jobin-Yvon LabRAM HR-800 Raman spectrometer. X-ray photoelectron spectroscopy (XPS) was obtained by using a ThermoFisher ESCALAB250xi.  $N_2$  adsorption/desorption measurements were performed by using a Quantachrome instrument (Quabrador SI-3MP) at 77 K.

### 2.5. Electrochemical tests

Electrochemical characterizations were carried out in Li-O<sub>2</sub> coin batteries, drilled with 3×Φ1.5 mm holes in the center of the cell pans in an evenly distributed pattern to allow O<sub>2</sub> passage, consisting of a Li foil anode, an electrolyte of 1 M LiTFSI in tetraethylene glycol dimethyl ether (TEGDME), and an O<sub>2</sub> electrode (10 mm in diameter). The O<sub>2</sub> electrodes with catalyst were prepared by casting a mixture containing as-prepared  $\gamma$ -Fe<sub>2</sub>O<sub>3</sub>/carbon nanocomposites (15 wt.%), Super P (75 wt.%) and PVDF (10 wt.%) on a Ni foam, followed by drying at 50 °C in a vacuum oven for 12h, and this electrode was marked as FOC-SP electrode in this paper. The same method was employed to prepare the pure Super P electrodes which consist of Super P (90 wt.%) and PVDF (10 wt.%). The mass loading of active materials (carbon + catalyst) is about 0.8 mg cm<sup>-2</sup>. The Li-O<sub>2</sub> cells were assembled in an Ar filled glove box (Universal 2440/750) in which oxygen and water contents were less than 1 ppm. The galvanostatic discharge/charge performance of the Li-O<sub>2</sub> battery was tested at a current density of 0.1-0.4 mA cm<sup>-2</sup> in the potential range from 2.0 to 4.3 V under a LAND CT2001A system. It is noted that the specific capacity was calculated based on the total mass of carbon and catalyst. Cyclic voltammetry (CV) were conducted by using Solartron 1470E electrochemical measurement system. CV tests were performed at a scan rate of 0.5 mV s<sup>-1</sup> in the voltage range from 2.0 to 4.3

V. The linear sweep voltammograms (LSV) were obtained at a scan rate of  $2 \text{ mV s}^{-1}$ . All measurements were conducted in 1 atm dry oxygen to avoid any negative effects of humidity and  $\text{CO}_2$ .

### 3. Results and discussion

Fe based metal organic frameworks, MIL-100-Fe with the formula of  $\text{Fe}_3\text{F}(\text{H}_2\text{O})_3\text{O}(\text{BTC})_2 \cdot n\text{H}_2\text{O}$ , was synthesized from the hydrothermal reaction. Powder X-ray diffraction was employed to identify lattice structure of MIL-100-Fe. The XRD pattern of MIL-100-Fe is illustrated in Fig. 1, which reveals the crystal structure of MIL-100-Fe clearly. Crystal faces for all the peaks were also identified based on the crystallographic data and XRD patterns of MIL-100-Fe were found to be accordance with the earlier literature [29, 30], confirming the successful synthesis of MIL-100-Fe.

The resultant products can be prepared by calcination of the as-made MIL-100-Fe, and XRD pattern tests were then performed accordingly to confirm the formation of  $\gamma\text{-Fe}_2\text{O}_3$ /carbon nanocomposites. The XRD patterns of the as-prepared pyrolysis products are shown in Fig. 2a. The diffraction peaks of the composites can be assigned to the lattice of  $\gamma\text{-Fe}_2\text{O}_3$  with the corresponding diffraction peaks of (2 2 0), (3 1 1), (4 0 0), (4 2 2), (5 1 1), (4 4 0) planes, according to standard JCPDS card no. 39-1346, which is similar to the result reported by Sun [31]. Especially, the appearance of some additional superstructure reflections (marked with an arrow) in the pattern corresponding diffraction peaks of (1 1 0), (1 1 1), (2 1 0), (2 1 1), (4 2 1) planes can distinguish the  $\gamma\text{-Fe}_2\text{O}_3$  with  $\text{Fe}_3\text{O}_4$  [31-33], which exhibits a similar XRD pattern to  $\gamma\text{-Fe}_2\text{O}_3$  [31]. But these superstructure reflections are sometimes unobvious. So it is difficult to clearly identify the  $\gamma\text{-Fe}_2\text{O}_3$  and  $\text{Fe}_3\text{O}_4$  phases from the XRD pattern alone [30, 34, 35]. Therefore, XPS analysis



was employed to further distinguish the  $\gamma\text{-Fe}_2\text{O}_3$  and  $\text{Fe}_3\text{O}_4$  phases [30, 34, 35]. The survey spectrum of the composites depicted in Fig. 2c shows several peaks implying the presence of carbon (C 1s), oxygen (O 1s, 2s) and iron (Fe 2P, 3p) elements, which come from the carbon and  $\gamma\text{-Fe}_2\text{O}_3$  in the nanocomposites, respectively [34, 36]. The high-resolution spectrum of Fe is given in Fig. 2d. The two peaks at 711.1 and 724.8 eV can be assigned to Fe  $2p_{3/2}$  and Fe  $2p_{1/2}$  electron binding energy, respectively, which is in good agreement with the literature and clearly shows the existence of  $\gamma\text{-Fe}_2\text{O}_3$  [37]. Moreover, the shakeup satellite structures were also observed at the higher binding energy sides of the main peaks, indicated by arrows. These satellite peaks are the fingerprints of the electronic structures of  $\text{Fe}^{3+}$  and indicate the absent of  $\text{Fe}^{2+}$ , which is similar to the reported literature [34, 36, 37]. These result confirm that the metal oxide in the nanocomposites we synthesized is  $\gamma\text{-Fe}_2\text{O}_3$ .

However, no obvious XRD peaks corresponding to the phases of carbon, which should be derived from the carbonization of organic ligands in MIL-100-Fe framework during the heat treatment under an inert atmosphere, can be seen in the XRD patterns. Thereby, the Raman spectrum of the  $\gamma\text{-Fe}_2\text{O}_3$ /carbon nanocomposites, as presented in Fig. 2b, was performed to verify the presence of the carbon. Two typical Raman bands of carbon were observed at 1332 and 1593  $\text{cm}^{-1}$  in Fig. 2b, corresponding to the “D band”, arising from the defects and disorder in carbonaceous solid, and “G band”, from the stretching mode of C-C bonds of structurally ordered graphite crystallites, respectively [38, 39]. This result indicates the coexistence of graphite (G) and disordered (D) amorphous carbon in the  $\gamma\text{-Fe}_2\text{O}_3$ /carbon nanocomposites, and verifies the partial graphitization of the as-obtained carbon in the composites. The intensity ratio of the “D band” to “G band”, also known as the “R-value”, reveals the amount of graphitic carbon in the

carbonaceous materials, and the degree of graphitization increases with the decline of the “R-value” [40, 41]. The “R-value” of the carbon in the as-prepared composites was calculated as 0.92, which is lower than the value reported in some literatures [41, 42]. Since the electrical conductivity of graphitic carbon is substantially higher than that of amorphous carbon, the partially graphitized carbon may possess good electronic conductivity [41, 43, 44]. So it is expected that the presence of partially graphitized carbon in the as-prepared nanocomposites facilitates the electron transport of the materials during OER and ORR process of Li-O<sub>2</sub> batteries, and the  $\gamma$ -Fe<sub>2</sub>O<sub>3</sub>/carbon nanocomposites might exhibit excellent electrocatalytic performances [15, 17-19]. All the results confirm that the  $\gamma$ -Fe<sub>2</sub>O<sub>3</sub>/carbon nanocomposites have been successfully synthesized via the pyrolysis of MIL-100-Fe.

In order to elucidate the mechanism of MIL-100-Fe thermal decomposition in an argon atmosphere, the degradation of the prepared Fe-containing MOFs was examined by thermogravimetric analysis (TGA). TGA curve, as shown in Fig. 3a, indicates that the sample encountered a initial weight loss of ~28 % when the temperature was increased from room temperature to 100 °C, corresponding to the elimination of adsorbed and bound water molecules. The material shows further drastic degradation at around 400 °C, which is ascribed to the partially decomposition of organic ligands in MIL-100-Fe framework [45]. The partially decomposition of organic ligands in MOF framework and the porosity of MOFs allows the formation of porous structure in the  $\gamma$ -Fe<sub>2</sub>O<sub>3</sub>/carbon nanocomposites. The weight of the sample finally stabilized at a temperature of ~500 °C when ~40 % by mass of the material was remained. This remained phase corresponds to the  $\gamma$ -Fe<sub>2</sub>O<sub>3</sub>/carbon nanocomposites described in this report. From the TGA curve of  $\gamma$ -Fe<sub>2</sub>O<sub>3</sub>/carbon nanocomposites shown in Fig. 3b, we find that the mass percentages of  $\gamma$ -Fe<sub>2</sub>O<sub>3</sub>

in the remained phase are ~65 wt%.

Morphological features of MIL-100-Fe and its derivative  $\gamma$ -Fe<sub>2</sub>O<sub>3</sub>/carbon nanocomposites were investigated through SEM and TEM, and presented in Fig. 4. The SEM image of MIL-100-Fe, shown in Fig. 4a, shows the octahedral structures of the MIL-100-Fe crystals with the size of ~400 nm. Fig. 4b clearly shows a large number of  $\gamma$ -Fe<sub>2</sub>O<sub>3</sub>/carbon nanocomposites secondary particles obtained after the pyrolysis of aforementioned MOFs at 600 °C which look octahedral in shape and have an average size of ~400 nm, similar to the starting morphology of MIL-100-Fe. It can be found that the surface of every such secondary particle is decorated by some nanoparticles with dimensions of ~20 nm which are confirmed to be  $\gamma$ -Fe<sub>2</sub>O<sub>3</sub> primary nanoparticles by TEM and HR-TEM images. The TEM and HR-TEM images of  $\gamma$ -Fe<sub>2</sub>O<sub>3</sub>/carbon nanocomposites showed in Fig. 4c and 4d give further evidence of the  $\gamma$ -Fe<sub>2</sub>O<sub>3</sub>/carbon nanocomposites secondary particles' hierarchical mesoporous nanostructure. We can observe that the as-prepared nanocomposites secondary particles are composed of porous carbon and  $\gamma$ -Fe<sub>2</sub>O<sub>3</sub> primary nanoparticles in a size range of <20 nm which are well dispersed in the composites. The uniform distribution of the  $\gamma$ -Fe<sub>2</sub>O<sub>3</sub> primary particles obtained after pyrolysis is due to the evenly distribution of metal ions in the parent MOFs ensure, and the robust MOF structures ensure reasonably good control over the  $\gamma$ -Fe<sub>2</sub>O<sub>3</sub> primary particle size. As shown in Fig. 4c, the as-prepared octahedral shaped nanocomposites secondary particles show a hierarchical mesoporous nanostructure, which is mainly formed by close-packed porous carbon and  $\gamma$ -Fe<sub>2</sub>O<sub>3</sub> primary nanoparticles. This hierarchical mesoporous nanostructure can be confirmed by Isothermal N<sub>2</sub> adsorption-desorption analysis. Nitrogen adsorption-desorption isotherms of the as-prepared nanocomposites are presented in Fig. 5. The composites exhibit typical IV N<sub>2</sub> sorption

isotherms with distinct H3 hysteresis loops which can be linked to slit-shaped pores, further suggesting its porous structure [16, 46]. As shown in the inset in Fig. 5, the pores of the  $\gamma\text{-Fe}_2\text{O}_3$ /carbon nanocomposites reveal a broad size distribution. In addition, the total specific surface area of the as-prepared composites, which is calculated by Brunauer-Emmett-Teller (BET) theory, is measured to be  $194.3 \text{ m}^2 \text{ g}^{-1}$ , which is much higher than the total specific surface area that was also calculated by Brunauer-Emmett-Teller (BET) theory of reported catalyst with similar nanostructure [15-17]. HR-TEM images given in Fig. 4d show distinct lattice fringes and the distance between two adjacent planes (d value) is found to be 0.25 nm which corresponds to (311) plane of the  $\gamma\text{-Fe}_2\text{O}_3$  crystal lattice. All the results demonstrate that the  $\gamma\text{-Fe}_2\text{O}_3$  primary nanoparticles are incorporated with the residual carbon obtained from the decomposition of organic ligands in MIL-100-Fe framework, resulting in the formation of hierarchical mesoporous  $\gamma\text{-Fe}_2\text{O}_3$ /carbon nanocomposites secondary particles. The unique nanostructure of the  $\gamma\text{-Fe}_2\text{O}_3$ /carbon nanocomposites endow them with larger electroactive surface area, more active sites, and higher electronic conductivity, that may improve the electrocatalytic performance and Li-O<sub>2</sub> battery performance [15-19].

In order to investigate the electrocatalytic activity of the  $\gamma\text{-Fe}_2\text{O}_3$ /carbon nanocomposites on the electrochemical properties of a Li-O<sub>2</sub> battery, Super-P carbon black O<sub>2</sub> electrodes with  $\gamma\text{-Fe}_2\text{O}_3$ /carbon nanocomposites (FOC-SP electrode) were prepared and tested in oxygen atmosphere at 2.0-4.3 V versus Li/Li<sup>+</sup>, and were compared with pure Super-P carbon black O<sub>2</sub> electrodes. The discharge and charge voltage profiles of the two different electrodes at a current density of  $0.1 \text{ mA cm}^{-2}$  in the voltage windows between 2.0 and 4.3 V is presented in Fig. 6a. The FOC-SP electrode delivers a discharge capacity of  $\sim 5900 \text{ mAh g}^{-1}_{\text{carbon+catalyst}}$  with a very stable

discharge voltage plateau of  $\sim 2.70$  V, which is higher than the pure Super-P electrode ( $\sim 3350$  mAh  $\text{g}^{-1}_{\text{carbon+catalyst}}$ , with a discharge voltage of  $\sim 2.64$  V) about 0.06V. The charge capacity of FOC-SP electrode is  $\sim 5300$  mAh  $\text{g}^{-1}_{\text{carbon+catalyst}}$ , which is almost the same as the discharge capacities. However, the pure Super-P electrode could not achieve good reversibility and only exhibits a charge capacity of  $\sim 2290$  mA h  $\text{g}^{-1}_{\text{carbon+catalyst}}$ . It should be noted that FOC-SP electrode also exhibits considerably low charge voltage for the OER process at  $\sim 3.75$  V vs.  $\text{Li/Li}^+$ , which is much lower than the pure Super-P carbon black electrode ( $\sim 4.1$  V) about 0.35V and is comparable to that of catalysts based on precious metals and is substantially lower than that of other reported carbon materials [5, 47, 48]. This result indicates that the overpotential of cells was reduced by  $\sim 0.41$  V with the addition of the catalyst we synthesized. Moreover, the discharge/charge voltage profiles shown in Fig. 6a reveal that the roundtrip efficiency, based on the charge-discharge capacity potential plateaus, of FOC-SP electrode is  $\sim 72\%$ , while pure Super-P carbon black electrode exhibits only 57.5 %. At higher current density, it is not surprising to observe that the discharge voltage decreased and the charge voltage increased with the increased current density, respectively, which results from the higher ohmic losses caused by the higher current density [49, 50]. We can also observe that the decrease of discharge capacity with the increase of applied current due to the oxygen diffusion limitation in nonaqueous electrolyte [49, 51, 52]. But FOC-SP electrode still shows much higher charge-discharge capacities than the pure Super-P carbon black electrode. The increased capacity, lower charge voltage plateau and higher discharge voltage plateau of the FOC-SP electrode could be attributed to the high catalytic activity of the  $\gamma\text{-Fe}_2\text{O}_3$ /carbon nanocomposites. This may be because the  $\gamma\text{-Fe}_2\text{O}_3$  has high intrinsic catalytic activity for ORR and OER [26-27], and the hierarchical mesoporous nanostructure of the

composites possesses larger electroactive surface area, thus facilitating the contact between the electrolyte and catalyst and providing more active sites [15-17]. Further more, the existence of the carbon in the composites ensures high electronic conductivity that is beneficial to transport of electrons during OER and ORR process [15, 17-19]. This unique structure and composition results the excellent electrocatalytic ability of the  $\gamma$ -Fe<sub>2</sub>O<sub>3</sub>/carbon nanocomposites.

Recently, it has been reported that limiting the charge and discharge capacities is a widely used method to improve the cycling stability of Li-O<sub>2</sub> batteries [53-55]. We also investigate the cycle stability of FOC-SP electrode with confining the discharge/charge capacities to 600 mA h g<sup>-1</sup><sub>carbon+catalyst</sub>, at a current density of 0.1 mA cm<sup>-2</sup> in the voltage windows between 2.0 and 4.4 V. As presented in Fig. 6b and 6c, FOC-SP electrode shows good cycle performance over 30 cycles with stable reversible capacities, and the charge potential rises slightly. As shown in Fig. 6b and 6d, the cell with pure Super-P electrode was also tested under the same capacity-limited discharge/charge mode for comparison, which clearly indicates that only a few cycles can be sustained. It should be noted that the charge voltages increase and the discharge voltages decrease dramatically for the pure Super-P carbon black electrode during the cycling. These facts clearly indicate that the addition of  $\gamma$ -Fe<sub>2</sub>O<sub>3</sub>/carbon nanocomposites can extremely improve the cycle stability of Li-O<sub>2</sub> batteries. This may be attributed to the efficient electrocatalytic activities of  $\gamma$ -Fe<sub>2</sub>O<sub>3</sub>/carbon nanocomposites. The cyclability of Li-O<sub>2</sub> batteries is largely affected by the instability of the electrolyte. At high potentials during charge process, the ether-based electrolyte will be oxidized by Li<sub>2</sub>O<sub>2</sub>. That will lead to the decomposition of the electrolyte and deteriorate the cyclability [53, 56, 57]. The catalyst can effectively reduce the charge potentials, so it can prevent the decomposition of TEGDME, and consequently enhance the cyclability [58-60].

In order to further explore the catalytic activity of  $\gamma$ -Fe<sub>2</sub>O<sub>3</sub>/carbon nanocomposites, the cyclic voltammograms (CVs) and linear sweep voltammograms (LSV) of Li-O<sub>2</sub> batteries with the two different cathodes were tested under an O<sub>2</sub> atmosphere, the results were shown in Fig. 7. As shown in Fig. 7a, the ORR onset potential of FOC-SP electrode was approximately 2.95 V vs. Li/Li<sup>+</sup>, which was close to the value reported for Fe<sub>2</sub>O<sub>3</sub> nanocluster-decorated graphene [18], and the ORR peak potential of FOC-SP electrode centering at ~2.65 V. Compared with the electrode without catalyst, FOC-SP electrode exhibits a higher ORR onset and peak potential and FOC-SP electrode also has a higher ORR peak current response. This result is consistent with the ORR polarization curves obtained from linear sweep voltammograms that was shown in Fig. 7b. The broad OER peak of FOC-SP electrode centering at ~3.75V vs. Li/Li<sup>+</sup> was attributed to the oxidation of Li<sub>2</sub>O<sub>2</sub>, while the peak potential of the electrode without catalyst is difficult to define. In the OER polarization curves obtained from linear sweep voltammograms that was shown in Fig. 7c, the FOC-SP electrode also exhibits an obviously higher OER current and lower onset potential. This result suggests that  $\gamma$ -Fe<sub>2</sub>O<sub>3</sub>/carbon nanocomposites can be an effective ORR and OER catalyst for Li-O<sub>2</sub> batteries [17, 61].

Since the formation of the high reactivity of the intermediate species during the oxygen reduction reaction (ORR) process, lithium superoxide, in lithium-O<sub>2</sub> batteries, the electrolytes, even the relative stable ether-based electrolytes, are still not completely stable in the Li-O<sub>2</sub> batteries system. And the decomposition of electrolytes may contribute to the capacity of lithium-O<sub>2</sub> batteries [62-64]. In order to make sure our cells' discharge and charge capacity with FOC-SP electrode are deriving from the generation and decomposition of Li<sub>2</sub>O<sub>2</sub>, which is the discharge product of Li-O<sub>2</sub> batteries, the ex-situ XRD test was performed. As presented in Fig. 8,

the XRD patterns of the fresh, discharged, and recharged electrodes were obtained, respectively. According to the XRD patterns, two typical peaks corresponded to the formation of  $\text{Li}_2\text{O}_2$  phase were observed at 33.1 and 34.8 °, after fully discharging the cell to 2.0 V at a current density of 0.1  $\text{mA cm}^{-2}$  [54, 55]. When the cell was fully recharged to 4.3 V, these two peaks related to the  $\text{Li}_2\text{O}_2$  phase were found to have fully disappeared, indicating that the  $\text{Li}_2\text{O}_2$  phase formed in the discharging process had been reversibly decomposed during the subsequent charging. The reversible formation and decomposition of  $\text{Li}_2\text{O}_2$  suggests that there is no obvious decomposition of the electrolyte during charge-discharge process in the Li-air batteries with FOC-SP electrode and, thus,  $\gamma\text{-Fe}_2\text{O}_3$ /carbon nanocomposites can function as both ORR and OER catalysts in Li- $\text{O}_2$  batteries.

#### 4. Conclusions

In summary, a hierarchical mesoporous  $\gamma\text{-Fe}_2\text{O}_3$ /carbon nanocomposites was synthesized by the pyrolysis of metal organic frameworks (MOFs) MIL-100(Fe). The electrochemical performance of  $\gamma\text{-Fe}_2\text{O}_3$ /carbon nanocomposites as cathode catalyst in Li- $\text{O}_2$  batteries was investigated. The electrode with  $\gamma\text{-Fe}_2\text{O}_3$ /carbon nanocomposites shows excellent electrochemical performances with a discharge capacity up to  $\sim 5970 \text{ mAh g}^{-1}_{\text{carbon+catalyst}}$  at 0.1  $\text{mA cm}^{-2}$  (125  $\text{mA g}^{-1}$ ) and a high C-rate performance with a discharge capacity of  $\sim 4130 \text{ mAh g}^{-1}_{\text{carbon+catalyst}}$  at 0.2  $\text{mA cm}^{-2}$  and  $\sim 2977 \text{ mAh g}^{-1}_{\text{carbon+catalyst}}$  at 0.4  $\text{mA cm}^{-2}$ . Compared with pure Super P electrode, the electrode with  $\gamma\text{-Fe}_2\text{O}_3$ /carbon nanocomposites exhibits a lower charge and discharge overpotential, higher discharge capacity and better cycling stability. The improved performance demonstrates that the as-synthesized hierarchical mesoporous  $\gamma\text{-Fe}_2\text{O}_3$ /carbon nanocomposites have an excellent electrocatalytic activity, indicating its potential as a promising catalyst for Li- $\text{O}_2$



batteries. Besides the high intrinsic electrocatalytic activity of  $\gamma\text{-Fe}_2\text{O}_3$  for ORR and OER, the excellent electrocatalytic activity of the composites may also be ascribed to the more active sites and the faster electron transport provided by the hierarchical mesoporous nanostructure and the existing carbon, respectively. Consequently, the  $\gamma\text{-Fe}_2\text{O}_3$ /carbon nanocomposites would be a promising electrocatalyst for Li-O<sub>2</sub> batteries. These results suggest that the present thermal decomposition of MOFs is a facile simple strategy to prepare porous nanocomposites materials as the catalyst for Li-O<sub>2</sub> batteries.

## References

- [1] Y. Wang, P. He, H. Zhou, A lithium-air capacitor-battery based on a hybrid electrolyte, *Energy Environ. Sci.* 4 (2011) 4994.
- [2] Y. C. Lu, B. M. Gallant, D. G. Kwabi, J. R. Harding, R. R. Mitchell, M. S. Whittingham, S. H. Yang, Lithium-oxygen batteries: bridging mechanistic understanding and battery performance, *Energy Environ. Sci.* 6 (2013) 750.
- [3] H. Ohkuma, I. Uechi, N. Imanishi, A. Hirano, Y. Takeda, O. Yamamoto, Carbon electrode with perovskite-oxide catalyst for aqueous electrolyte lithium-air secondary batteries, *J. Power Sources* 223 (2013) 319.
- [4] H.- G. Jung, Y. S. Jeong, J.- B. Park, Y.- K. Sun, B. Scrosati, Y. J. Lee, Ruthenium-based electrocatalysts supported on reduced graphene oxide for lithium-air batteries, *ACS Nano* 7 (2013) 3532.
- [5] Y. C. Lu, Z. Xu, H. A. Gasteiger, S. Chen, K. Hamad-Schifferli, Y. Shao-Horn, Platinum-Gold nanoparticles: a highly active bifunctional electrocatalyst for rechargeable lithium-air batteries, *J. Am. Chem. Soc.* 132 (2010) 12170.

- [6] P. G. Bruce, S. A. Freunberger, L. J. Hardwick, J. M. Tarascon, Li-O<sub>2</sub> and Li-S batteries with high energy storage, *Nat. Mater.* 11 (2011) 19.
- [7] Y. C. Lu, H. A. Gasteiger, E. Crumlin, R. McGuire, Y. Shao-Horn, Electrocatalytic activity studies of select metal surfaces and implications in Li-air batteries, *J. Electrochem. Soc.* 157 (2010) A1016.
- [8] Y. C. Lu, H. A. Gasteiger, M. C. Parent, V. Chiloyan, Y. Shao-Horn, The influence of catalysts on discharge and charge voltages of rechargeable Li-oxygen batteries, *Electrochem. Solid State Lett.* 13 (2010) A69.
- [9] J. R. Harding, Y. C. Lu, Y. Tsukada, Y. Shao-Horn, Evidence of catalyzed oxidation of Li<sub>2</sub>O<sub>2</sub> for rechargeable Li-air battery applications, *Phys.Chem. Chem. Phys.* 14 (2012) 10540.
- [10] T. Ogasawara, A. Debart, M. Holzapfel, P. Novak, P. G. Bruce, Rechargeable Li<sub>2</sub>O<sub>2</sub> electrode for lithium batteries, *J. Am. Chem. Soc.* 128 (2006) 1390.
- [11] A. Debart, A. J. Paterson, J. Bao, P. G. Bruce,  $\alpha$ -MnO<sub>2</sub> nanowires: a catalyst for the O<sub>2</sub> electrode in rechargeable lithium batteries, *Angew. Chem.* 120 (2008) 4597.
- [12] A. Debart, J. Bao, G. Armstrong, P. G. Bruce, An O<sub>2</sub> cathode for rechargeable lithium batteries: the effect of a catalyst, *J. Power Sources* 174 (2007) 1177.
- [13] A. K. Thapa, K. Saimen, T. Ishihara, Pd / MnO<sub>2</sub> air electrode catalyst for rechargeable lithium/air battery, *Electrochem. Solid State Lett.* 13 (2010) A165.
- [14] A. K. Thapa, T. Ishihara, Mesoporous  $\alpha$ -MnO<sub>2</sub>/Pd catalyst air electrode for rechargeable lithium-air battery, *J. Power Sources* 196 (2011) 7016.
- [15] S. H. Oh, R. Black, E. Pomerantseva, J.- H. Lee, L. F. Nazar, Synthesis of a metallic mesoporous pyrochlore as a catalyst for lithium-O<sub>2</sub> batteries, *Nature Chemistry* 4 (2012)

1004.

- [16] Y. Zhao, L. Xu, L. Mai, C. Han, Q. An, X. Xu, X. Liu, Q. Zhang, Hierarchical mesoporous perovskite  $\text{La}_{0.5}\text{Sr}_{0.5}\text{CoO}_{2.91}$  nanowires with ultrahigh capacity for Li-air batteries, PNAS 109 (2012) 19569.
- [17] K. Zhang, L. Zhang, X. Chen, X. He, X. Wang, S. Dong, L. Gu, Z. Liu, C. Huang, G. Cui. Molybdenum nitride/N-doped carbon nanospheres for lithium- $\text{O}_2$  battery cathode electrocatalyst, ACS Appl. Mater. Interfaces 5 (2013) 3677.
- [18] W. Zhang, Y. Zeng, C. Xu, H. Tan, W. Liu, J. Zhu, N. Xiao, H. H. Hng, J. Ma, H. E. Hoster, R. Yazami, Q. Yan,  $\text{Fe}_2\text{O}_3$  nanocluster-decorated graphene as  $\text{O}_2$  electrode for high energy Li- $\text{O}_2$  batteries, RSC Adv. 2 (2012) 8508.
- [19] Y. Cao, Z. Wei, J. He, J. Zang, Q. Zhang, M. Zheng, Q. Dong,  $\alpha\text{-MnO}_2$  nanorods grown in situ on graphene as catalysts for Li- $\text{O}_2$  batteries with excellent electrochemical performance, Energy Environ. Sci. 5 (2012) 9765.
- [20] R. Banerjee, A. Phan, B. Wang, C. Knobler, H. Furukawa, M. O'Keeffe, O.M. Yaghi, High-throughput synthesis of zeolitic imidazolate frameworks and application to  $\text{CO}_2$  capture, Science 319 (2008) 939.
- [21] M. Alvaro, E. Carbonell, B. Ferrer, F. X. Llabrés Xamena, H. Garcia, Semiconductor behavior of a metal-organic framework (MOF), Chemistry A European Journal 13 (2007) 5106.
- [22] C. D. Wu, A. Hu, L. Zhang, W. Lin, A homochiral porous metal-organic framework for highly enantioselective heterogeneous asymmetric catalysis, J. Am. Chem. Soc. 127 (2005) 8940.
- [23] S. J. Yang, T. Kim, J. H. Im, Y. S. Kim, K. Lee, H. Jung, C. R. Park. MOF-derived

- hierarchically porous carbon with exceptional porosity and hydrogen storage capacity, *Chem. Mater.* 24 (2012) 464.
- [24] X. Xu, R. Cao, S. Jeong, J. Cho, Spindle-like mesoporous  $\alpha$ -Fe<sub>2</sub>O<sub>3</sub> anode material prepared from MOF template for high-rate lithium batteries, *Nano Lett.* 12 (2012) 4988.
- [25] J. Lu, Y. Qin, P. Du, X. Luo, T. Wu, Y. Ren, J. Wen, D. J. Miller, J. T. Miller, K. Amine, Synthesis and characterization of uniformly dispersed Fe<sub>3</sub>O<sub>4</sub>/Fe nanocomposite on porous carbon: application for rechargeable Li-O<sub>2</sub> batteries, *RSC Adv.* 3 (2013) 8276.
- [26] B. C. Hixson, J. W. Jordan, E. L. Wagner, H. M. Bevsek, Reaction products and kinetics of the reaction of NO<sub>2</sub> with  $\gamma$ -Fe<sub>2</sub>O<sub>3</sub>, *J. Phys. Chem. A* 115 (2011) 13364.
- [27] B. Wang, J.-J. Yin, X. Zhou, I. Kurash, Z. Chai, Y. Zhao, W. Feng, Physicochemical origin for free radical generation of iron oxide nanoparticles in biomicroenvironment: catalytic activities mediated by surface chemical states, *J. Phys. Chem. C* 117 (2013) 383.
- [28] E. Soubeyrand-Lenoir, C. Vagner, J. W. Yoon, P. Bazin, F. Ragon, Y. K. Hwang, C. Serre, J.-S. Chang, P. L. Llewellyn, How water fosters a remarkable 5-fold increase in low pressure CO<sub>2</sub> uptake within the mesoporous MIL-100(Fe), *J. Am. Chem. Soc.* 134 (2012) 10174.
- [29] Y. Xu, L. Xu, S. Qi, Y. Dong, Z. Rahman, H. Chen, X. Chen, In situ synthesis of MIL-100(Fe) in the capillary column for capillary electrochromatographic separation of small organic molecules, *Anal. Chem.* 85 (2013) 11369.
- [30] J. D. Xiao, L. G. Qiu, X. Jiang, Y. J. Zhu, S. Ye, X. Jiang, Magnetic porous carbons with high adsorption capacity synthesized by a microwave-enhanced high temperature ionothermal method from a Fe-based metal-organic framework, *Carbon* 59 (2013) 372.

- [31] J. Jørgensen, L. Mosegaard, L. E. Thomsen, T. R. Jensen, J. C. Hanson, Formation of  $\gamma$ -Fe<sub>2</sub>O<sub>3</sub> nanoparticles and vacancy ordering: An in situ X-ray powder diffraction study, *J. Solid State Chemistry* 180 (2007) 180.
- [32] G. Sun, B. Dong, M. Cao, B. Wei, C. Hu, Hierarchical dendrite-like magnetic materials of Fe<sub>3</sub>O<sub>4</sub>,  $\gamma$ -Fe<sub>2</sub>O<sub>3</sub>, and Fe with high performance of microwave absorption, *Chem. Mater.* 23 (2011) 1587.
- [33] M. P. Morales, S. Veintemillas-Verdaguer, M. I. Montero, C. J. Serna, Surface and internal spin canting in  $\gamma$ -Fe<sub>2</sub>O<sub>3</sub> nanoparticles, *Chem. Mater.* 11 (1999) 3058.
- [34] Y. Liu, L. Yu, Y. Hu, C. Guo, F. Zhang, X. W. (David) Lou, A magnetically separable photocatalyst based on nest-like  $\gamma$ -Fe<sub>2</sub>O<sub>3</sub>/ZnO double-shelled hollow structures with enhanced photocatalytic activity, *Nanoscale* 4 (2012) 183.
- [35] Y. Chen, F. Zhang, G. Zhao, X. Fang, H. Jin, P. Gao, C. Zhu, M. Cao, G. Xiao, Synthesis, multi-nonlinear dielectric resonance, and excellent electromagnetic absorption characteristics of Fe<sub>3</sub>O<sub>4</sub>/ZnO core/shell nanorods, *J. Phys. Chem. C* 114 (2010) 9239.
- [36] P. Wu, N. Du, H. Zhang, L. Jin, D. Yang, Functionalization of ZnO nanorods with  $\gamma$ -Fe<sub>2</sub>O<sub>3</sub> nanoparticles: Layer-by-layer synthesis, optical and magnetic properties, *Materials Chemistry and Physics* 124 (2010) 908.
- [37] M. Descostes, F. Mercier, N. Thomat, C. Beaucaire, M. Gautier-Soyer, Use of XPS in the determination of chemical environment and oxidation state of iron and sulfur samples: constitution of a data basis in binding energies for Fe and S reference compounds and applications to the evidence of surface species of an oxidized pyrite in a carbonate medium, *Applied Surface Science* 165 (2000) 288.

- [38] J. Li, B. Peng, G. Zhou, Z. Zhang, Y. Lai, M. Jia, Partially cracked carbon nanotubes as cathode materials for lithium-air batteries, *ECS Electrochemistry Letters* 2 (2013) A25.
- [39] J. Robertson, Diamond-like amorphous carbon, *Mater. Sci. Eng. R* 37 (2002) 129.
- [40] M. Endo, C. Kim, T. Karaki, T. Kasai, Structural characterization of milled mesophase pitch-based carbon fibers, *Carbon* 36 (1998) 1633.
- [41] L. Hou, L. Lian, D. Li, G. Pang, J. Li, X. Zhang, S. Xiong, C. Yuan, Mesoporous N-containing carbon nanosheets towards high-performance electrochemical capacitors, *Carbon* 64 (2013) 141.
- [42] Y. Qu, Z. Zhang, X. Wang, Y. Lai, Y. Liu, J. Li, A simple SDS-assisted self-assembly method for the synthesis of hollow carbon nanospheres to encapsulate sulfur for advanced lithium-sulfur batteries, *J. Mater. Chem. A* 1 (2013) 14306.
- [43] P. F. Fulvio, R. T. Mayes, X. Wang, S. M. Mahurin, J. C. Bauer, V. Presser, J. McDonough, Y. Gogotsi, S. Dai, “Brick-and-Mortar” self-assembly approach to graphitic mesoporous carbon nanocomposites, *Adv. Funct. Mater.* 21 (2011) 2208.
- [44] D. Wang, F. Li, M. Liu, G. Q. Lu, H. Cheng, 3D aperiodic hierarchical porous graphitic carbon material for high-rate electrochemical capacitive energy storage, *Angew. Chem. Int. Ed.* 47 (2008) 373.
- [45] L. Chen, J. Bai, C. Wang, Y. Pan, M. Scheer, X. You, One-step solid-state thermolysis of a metal-organic framework: a simple and facile route to large-scale of multiwalled carbon nanotubes, *Chem. Commun.* 13 (2008) 1581.
- [46] W. Zhu, Z. Liang, X. Liu, H. Zhang, Y. Zheng, X. Piao, Q. Zhang, Soft-template self-assembly of hierarchical mesoporous  $\text{SrCO}_3$  by low-temperature hydrothermal route and

- their application as adsorbents for methylene blue and heavy metal ions, *Powder Technology* 226 (2012) 165.
- [47] B. Sun, B. Wang, D. Su, L. Xiao, H. Ahn, G. Wang. Graphene nanosheets as cathode catalysts for lithium-air batteries with an enhanced electrochemical performance, *Carbon* 50 (2012) 727.
- [48] S. H. Oh, L. F. Nazar. Oxide catalysts for rechargeable high-capacity Li-O<sub>2</sub> batteries, *Adv. Energy Mater.* 2 (2012) 903.
- [49] C. Xia, M. Waletzko, K. Peppler, J. Janek, Silica nanoparticles as structural promoters for oxygen cathodes of lithium-oxygen batteries, *J. Phys. Chem. C* 117 (2013) 19897.
- [50] C. Xia, C. L. Bender, B. Bergner, K. Peppler, J. Janek, An electrolyte partially-wetted cathode improving oxygen diffusion in cathodes of non-aqueous Li-air batteries, *Electrochem. Commun.* 26 (2013) 93.
- [51] V. Viswanathan, K. S. Thygesen, J. S. Hummelshøj, J. K. Nørskov, G. Girishkumar, B. D. McCloskey, A. C. Luntz, Electrical conductivity in Li<sub>2</sub>O<sub>2</sub> and its role in determining capacity limitations in non-aqueous Li-O<sub>2</sub> batteries, *J. Chem. Phys.* 135 (2011) 214704(1-10).
- [52] Y. C. Lu, Y. Shao-Horn, Probing the reaction kinetics of the charge reactions of nonaqueous Li-O<sub>2</sub> batteries, *J. Phys. Chem. Lett.* 4 (2013) 93.
- [53] K. Song, J. Jung, Y.- U. Heo, Y. C. Lee, K. Cho, Y.- M. Kang,  $\alpha$ -MnO<sub>2</sub> nanowire catalysts with ultra-high capacity and extremely low overpotential in lithium-air batteries through tailored surface arrangement, *Phys. Chem. Chem. Phys.* 15 (2013) 20075.
- [54] B. Sun, J. Zhang, P. Munroe, H.- J. Ahn, G. Wang, Hierarchical NiCo<sub>2</sub>O<sub>4</sub> nanorods as an efficient cathode catalyst for rechargeable non-aqueous Li-O<sub>2</sub> batteries, *Electrochem.*

Commun. 31 (2013) 88.

- [55] W.- H. Ryu, T.- H. Yoon, S. H. Song, S. Jeon, Y.- J. Park, I.- D. Kim, Bifunctional composite catalysts using  $\text{Co}_3\text{O}_4$  nanofibers immobilized on nonoxidized graphene nanoflakes for high-capacity and long-cycle Li- $\text{O}_2$  batteries, *Nano Lett.* 13 (2013) 4190.
- [56] H. Wang, Y. Yang, Y. Liang, G. Zheng, Y. Li, Y. Cui, H. Dai, Rechargeable Li- $\text{O}_2$  batteries with a covalently coupled  $\text{MnCo}_2\text{O}_4$ -graphene hybrid as an oxygen cathode catalyst, *Energy Environ. Sci.* 5 (2012) 7931.
- [57] B. D. McCloskey, D. S. Bethune, R. M. Shelby, G. Girishkumar, A. C. Luntz, Solvents' critical role in nonaqueous lithium oxygen battery electrochemistry, *J. Phys. Chem. Lett.* 2 (2011) 1161.
- [58] C. S. Park, K. S. Kim, Y. J. Park, Carbon-sphere/ $\text{Co}_3\text{O}_4$  nanocomposite catalysts for effective air electrode in Li/air batteries, *J. Power Sources* 244 (2013) 72.
- [59] T. H. Yoon, Y. J. Park, Polydopamine-assisted carbon nanotubes/ $\text{Co}_3\text{O}_4$  composites for rechargeable Li-air batteries, *J. Power Sources* 244 (2013) 344.
- [60] Y. Qin, J. Lu, P. Du, Z. Chen, Y. Ren, T. Wu, J. T. Miller, J. Wen, D. J. Miller, Z. Zhang, K. Amine, In situ fabrication of porous-carbon-supported  $\alpha$ - $\text{MnO}_2$  nanorods at room temperature: application for rechargeable Li- $\text{O}_2$  batteries, *Energy Environ. Sci.* 6 (2013) 519.
- [61] Y. C. Lu, H. A. Gasteiger, S. H. Yang, Method development to evaluate the oxygen reduction activity of high-surface-area catalysts for Li-air batteries, *Electrochem and Solid-State Lett.* 14 (2011) A70.
- [62] B. Sun, X. Huang, S. Chen, J. Zhang, G. Wang, An optimized  $\text{LiNO}_3$ /DMSO electrolyte for high-performance rechargeable Li- $\text{O}_2$  batteries, *RSC Adv.* 4 (2014) 11115.



- [63] W. Xu, J. Hu, M. H. Engelhard, S. A. Towne, J. S. Hardy, J. Xiao, J. Feng, M. Y. Hu, J. Zhang, F. Ding, M. E. Gross, J. Zhang, The stability of organic solvents and carbon electrode in nonaqueous Li-O<sub>2</sub> batteries, *J. Power Sources* 215 (2012) 240.
- [64] N. Mozhzhukhina, L. P. Méndez, D. Leo, E. J. Calvo, Infrared spectroscopy studies on stability of dimethyl sulfoxide for application in a Li-air battery, *J. Phys. Chem. C* 117 (2013) 18375.

## Figure captions

**Fig.1.** XRD patterns of the as-synthesized MIL-100(Fe).

**Fig.2.** (a) XRD patterns of the as-synthesized  $\gamma$ -Fe<sub>2</sub>O<sub>3</sub>/Carbon nanocomposites; (b) Raman spectra of the as-synthesized  $\gamma$ -Fe<sub>2</sub>O<sub>3</sub>/carbon nanocomposites; and XPS spectrum of the as-prepared  $\gamma$ -Fe<sub>2</sub>O<sub>3</sub>/carbon nanocomposites: (c) survey spectrum, and (d) high-resolution Fe(2p) binding energy spectrum, showing the composition of  $\gamma$ -Fe<sub>2</sub>O<sub>3</sub>.

**Fig.3.** Thermogravimetric analysis (TGA) of (a) MIL-100(Fe) under N<sub>2</sub> atmosphere; (b)  $\gamma$ -Fe<sub>2</sub>O<sub>3</sub>/carbon nanocomposites under air atmosphere.

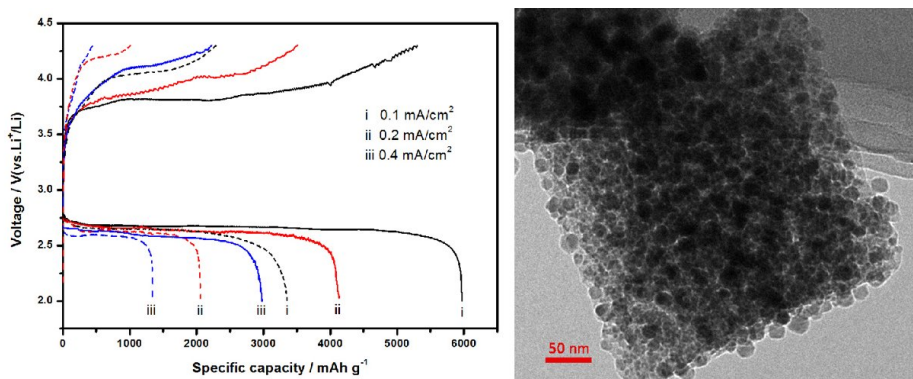
**Fig.4.** (a) SEM image of the as-synthesized MIL-100(Fe); (b) SEM image of the as-synthesized  $\gamma$ -Fe<sub>2</sub>O<sub>3</sub>/carbon nanocomposites; (c) TEM image and (d) HTEM image of the as-synthesized  $\gamma$ -Fe<sub>2</sub>O<sub>3</sub>/carbon nanocomposites.

**Fig.5.** The nitrogen adsorption/desorption isotherm of the as-synthesized  $\gamma$ -Fe<sub>2</sub>O<sub>3</sub>/carbon nanocomposites and the inset is the pore size distribution.

**Fig.6.** (a) Charge/discharge voltage curves of the Super-P carbon black air electrode with  $\gamma$ -Fe<sub>2</sub>O<sub>3</sub>/carbon nanocomposites (solid line) and the pure Super-P carbon black electrode (dash line) at different current densities; (b) Cyclic performance of the air electrode measured under specific capacity limit of 600 mAh g<sup>-1</sup> as in the voltage window between 4.4 and 2.0 V at a current density of 0.1 mA cm<sup>-2</sup>; and charge and discharge behavior of (c) the Super-P carbon black air electrode with  $\gamma$ -Fe<sub>2</sub>O<sub>3</sub>/carbon nanocomposites and (d) the pure Super-P carbon black electrode with the curtailing capacity of 600 mAh g<sup>-1</sup> as in the voltage window between 4.4 and 2.0 V at a current density of 0.1 mA cm<sup>-2</sup>.

**Fig.7.** (a) CV curves of Li-O<sub>2</sub> batteries with and without  $\gamma$ -Fe<sub>2</sub>O<sub>3</sub>/carbon nanocomposites at a scan rate of 0.5 mV s<sup>-1</sup>; (b) linear sweep voltammetry curves of ORR; and (c) linear sweep voltammograms of OER Li-O<sub>2</sub> batteries with  $\gamma$ -Fe<sub>2</sub>O<sub>3</sub>/carbon nanocomposites at a scan rate of 2 mV s<sup>-1</sup>.

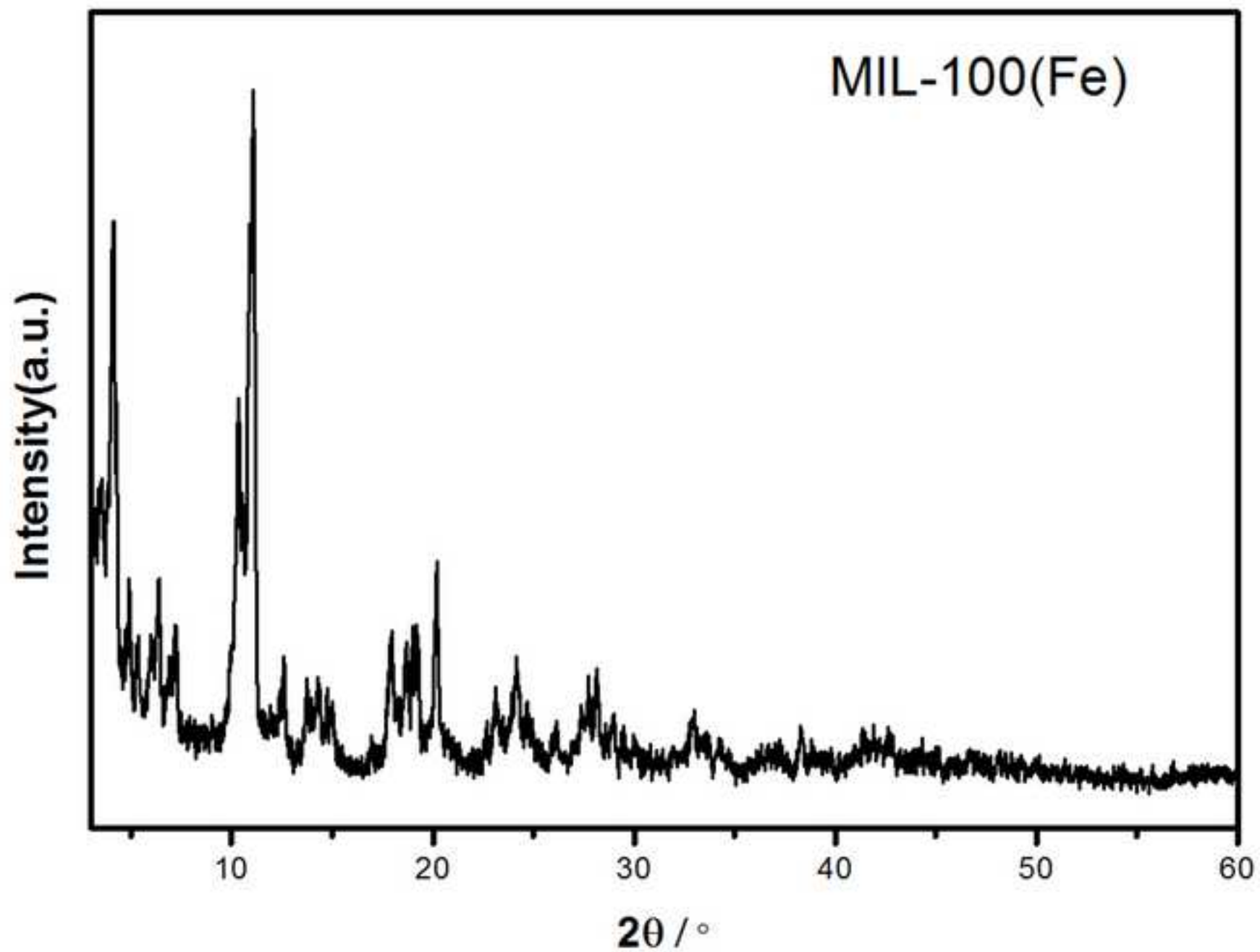
**Fig.8.** XRD patterns of fresh, discharged, and subsequent recharged Super-P electrode with  $\gamma$ -Fe<sub>2</sub>O<sub>3</sub>/carbon nanocomposites.

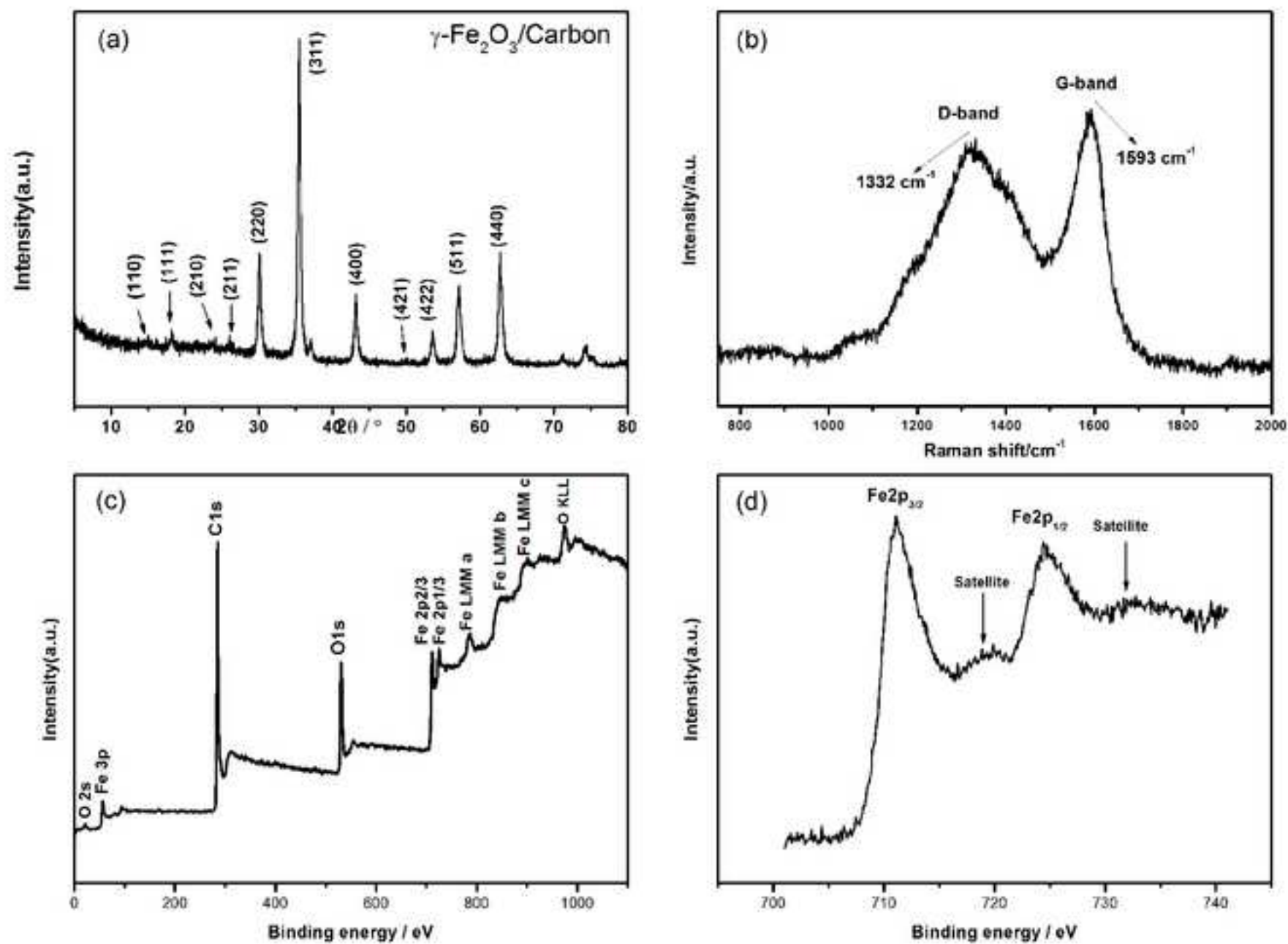


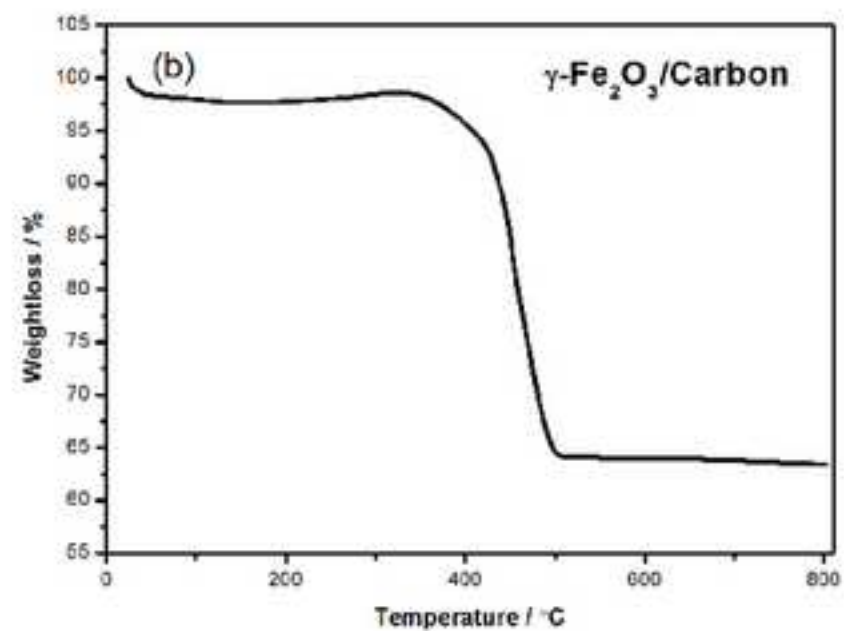
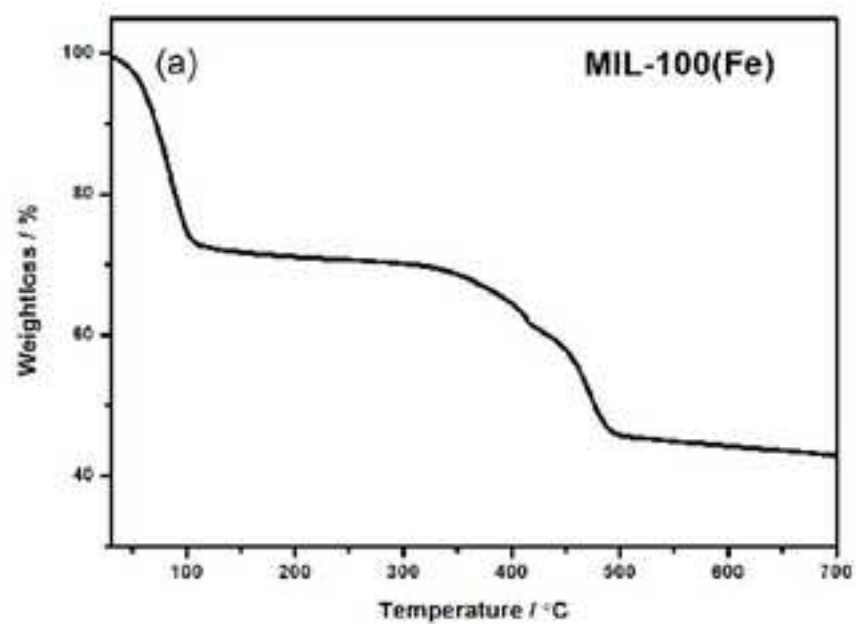
The hierarchical mesoporous  $\gamma\text{-Fe}_2\text{O}_3$ /carbon nanocomposites were prepared by the pyrolysis of metal organic frameworks (MOFs). Moreover, when the hierarchical mesoporous  $\gamma\text{-Fe}_2\text{O}_3$ /carbon nanocomposites were applied in Li-O<sub>2</sub> batteries as electrocatalyst, it exhibits an excellent electrocatalytic activity for both ORR and OER processes, which reveals a lower charge and discharge over-potential and considerable rate capability and cyclic ability. Besides the high intrinsic electrocatalytic activity of  $\gamma\text{-Fe}_2\text{O}_3$  for ORR and OER, the excellent electrocatalytic activity of the composites may also be ascribed to the more active sites and the faster electron transport provided by the hierarchical mesoporous nanostructure and the residual carbon, respectively.

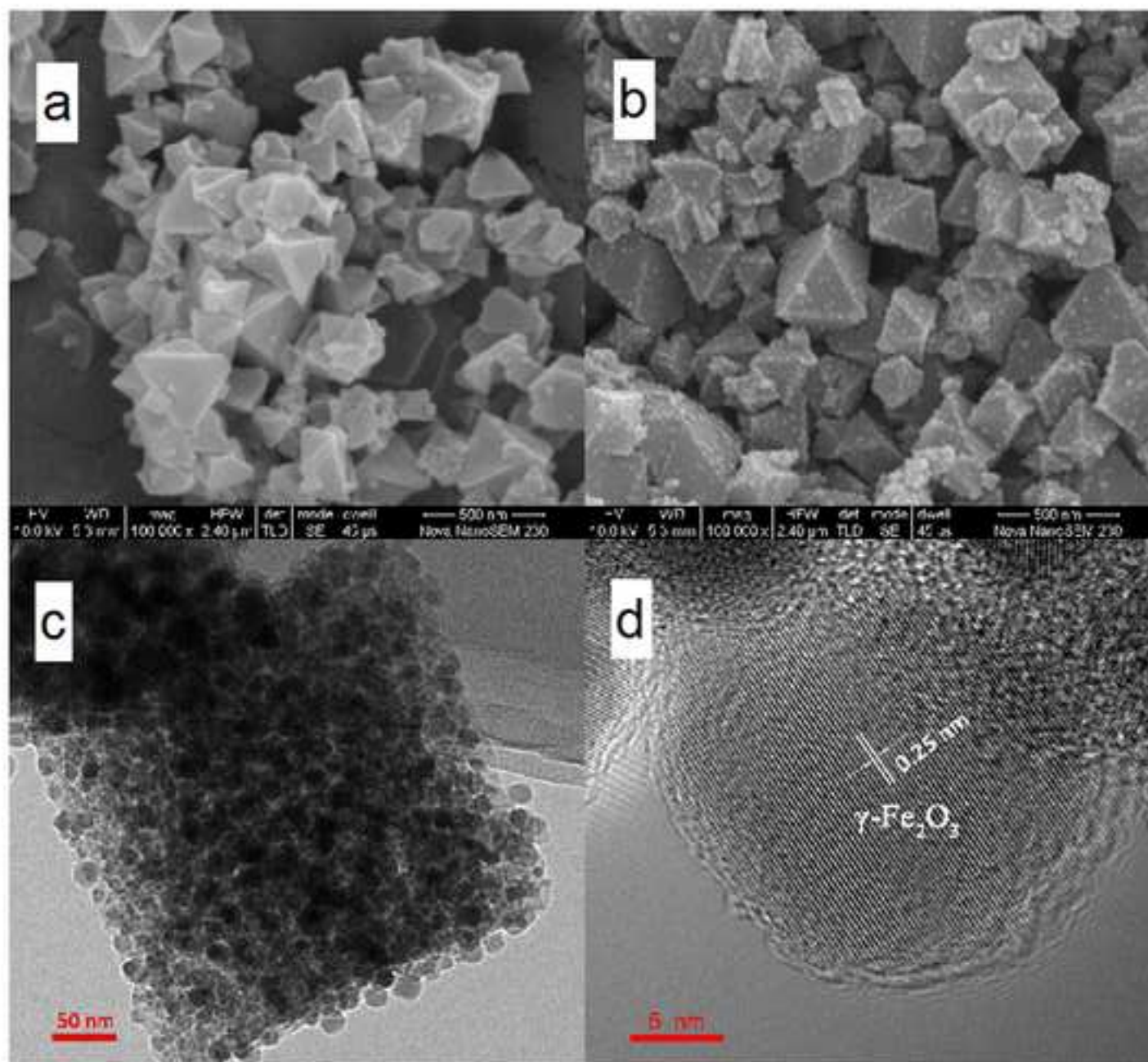
**Highlights:**

- The  $\gamma$ -Fe<sub>2</sub>O<sub>3</sub>/carbon nanocomposites were prepared by the pyrolysis of MOFs.
- The  $\gamma$ -Fe<sub>2</sub>O<sub>3</sub>/carbon nanocomposites have hierarchical mesoporous nanostructure.
- The  $\gamma$ -Fe<sub>2</sub>O<sub>3</sub> nanoparticles are well dispersed in composites.
- The  $\gamma$ -Fe<sub>2</sub>O<sub>3</sub>/carbon nanocomposites exhibit an excellent electrocatalytic activity.
- This work will be also of interest for other applications, such as supercapacitor.

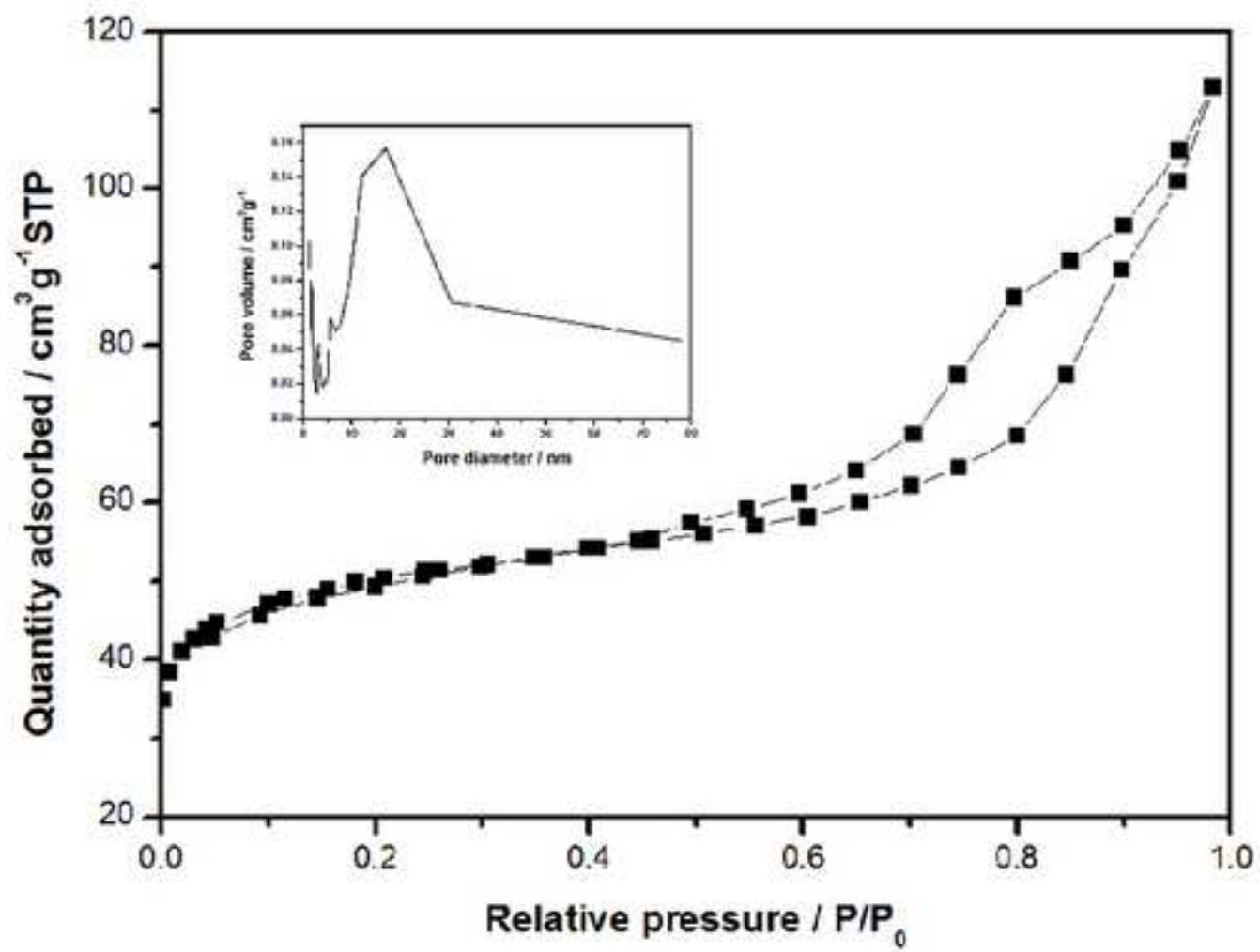












Figure(s)

